Epidemics 52 (2025) 100843

Contents lists available at ScienceDirect

Epidemics

journal homepage: www.elsevier.com/locate/epidemics

Modelling the dynamics of SARS-CoV-2 during the first 14 days of infection

Jingsi Xu [a],*, Martín López-García [b], Thomas House [a], Ian Hall [a]

[a] Department of Mathematics, University of Manchester, United Kingdom
[b] School of Mathematics, University of Leeds, United Kingdom

ARTICLE INFO

Keywords:
Within-host models
Dose-response
SARS-coV-2

ABSTRACT

Interpreting the viral mechanism of SARS-CoV-2 based on the human body level is critical for developing more efficient interventions. Due to the limitation of data, limited models consider the viral dynamics of the early phase of infection. The Human Challenge Study (Killingley et al., 2022) enables us to obtain data from inoculation to the 14th day after infection, which provides an overview of the dynamics of SARS-CoV-2 infection within the host. In the Human Challenge Study, each volunteer was inoculated with 10TCID50, approximately 55PFU, of a wild-type of virus (Killingley et al., 2022), and the data indicates that the viral load reduced below the detectable level within a day.

The simplified within-host models developed by Xu et al. (2023) explain the data from the Human Challenge Study (Killingley et al., 2022). However, they do not explain the viral decay from Day 0 to Day 1. Hence, in this paper, we aim to develop a new viral mechanism to explain this phenomenon. Based on the simplified within-host models developed by Xu et al. (2023), we consider that the virus will first go through an adjustment phase and then start to replicate. A new dose-response model is developed to evaluate the probability of infection by constructing a boundary problem. We will discuss this viral mechanism and fit the model to the data of the Human Challenge Study (Killingley et al., 2022) by adopting AMC-SMC (approximate Bayesian computation-sequential Monte Carlo). Based on the results of parameter inference, we estimate that the adjusted viral load is around 1% of the inoculated viral load.

1. Introduction

Since the pandemic of SARS-CoV-2, many studies have reported different within-host models aiming to introduce and explain different viral mechanisms (see e.g. Challenger et al. (2022), Goyal et al. (2020), Gonçalves et al. (2021), Li et al. (2022), Ghosh (2021), Sadria and Layton (2021), Du and Yuan (2020), Hernandez-Vargas and Velasco-Hernandez (2020), Abuin et al. (2020), Li et al. (2020), and Wang et al. (2020)). Understanding different models of viral mechanisms can offer more insights into considering targeted and effective intervention to limit the spread of SARS-CoV-2 and other respiratory diseases.

The Human Challenge Study (Killingley et al., 2022), abbreviated hereafter to HCS, measured the detectable viral load in the upper respiratory tract. In the study, 34 young male volunteers who were between 18–29 years old and had not been previously vaccinated or infected were given 10TCID50 of a wild type of virus, where 10TCID50 is approximately 55PFU with credible interval (Killingley et al., 2022). A few days after the inoculation, the viral load is observed to drop below the detectable level, 5PFU, subsequently growing above the detectable level. The length of days under detectable level thus varies from mid-turbinate to throat. The throat data shows a shorter period ranging from 1 day to 3 days with a mean of 2.5 days while the mid-turbinate ranges between 2 days to 8 days with a mean of 3.7 days. Previous work developed a simplified within-host model, Xu et al. (2023), assuming two mechanisms for the decay of viral load, (1) by the depletion of susceptible cells and (2) the adaptive immune response respectively, both of which explain the HCS data well separately and in combination. However, this model does not explain the early viral decay and so does not use the initial dose from HCS. In this paper, we investigate a viral mechanism to explain the earlier low viral load measures and extend the models of Xu et al. (2023) to consider an adaptive immune response growing logistically rather than a fast switch.

As we are using data from HCS rather than seeking to model the onset of symptoms (or infectiousness) explicitly (i.e. modelling the incubation or latent periods) we define early infection as the time before detectable viral load is measured. It has been reasonably suggested that an 'eclipse phase' may be added into the SIV model system to help explain the early decay of the viral load, in which the susceptible cells first become infected cells in the eclipse phase and then switch to productively infected cells (cf. Wang et al. (2020)). In another

* Corresponding author.
E-mail address: jingsi.xu@manchester.ac.uk (J. Xu).

https://doi.org/10.1016/j.epidem.2025.100843
Received 13 February 2025; Received in revised form 29 June 2025; Accepted 6 July 2025
Available online 22 July 2025

study based on HCS data (Iyaniwura et al., 2024), infection is initiated when one targeted cell enters the eclipse phase as the viral load that triggers infection is unknown, and the authors incorporate detailed biological mechanisms to interpret the viral dynamics. There are many other studies that consider the eclipse phase (cf. Hernandez-Vargas and Velasco-Hernandez (2020), Beauchemin et al. (2008), Holder et al. (2011), Madelain et al. (2018), Williams et al. (2024) and Baccam et al. (2006)). This may be a biological reality but is likely on a timescale faster than the cadence of data collection from cases recruited to studies.

Moreover, as (Iyaniwura et al., 2024) points out, there may be a gap between the inoculation and the start of exponential growth. Wu et al. (2023) conducts an air–liquid interface culture of human nasal epithelium and notes that, despite plenty of virus initially present, only a very small fraction of cells were infected, nearly 3% by 24 h post-inoculation, but by 48 h post-infection nearly 80% of ciliated cells became infected. This two-step infection pattern indicates an initial period of viral 'adjustment' or 'trapping', followed by a surge of productive infection. Hence, different from the concept that viral growth starts immediately upon inoculation just with a delay caused by the eclipse phase and independent of initial dose, our core assumption here is that during the first few days after the exposure, there is a period of viral 'adjustment' linked to initial dose. Specifically, we assume that there exists a relatively short period after the inoculation, during which the viral load will only decay. After this period, the virus will have adjusted to the human body and start to replicate. There are then two processes that may cause an individual to not become infected upon exposure. Firstly the given exposed viral load may decay to extinction during the adjustment phase. Secondly, the residual viral load will have a chance of 'fading out' during the replication phase prior to 'infection'. Therefore, we can develop a dose–response model to estimate the chance of infection.

The viral load of SARS-CoV-2 has been linked to the degree of disease severity, infectiousness, lung damage and transmission risk (see e.g. Fajnzylber et al. (2020), Williamson et al. (2020) and Pujadas et al. (2020)) though the HCS found limited evidence of viral load corresponding to more severe infection (Killingley et al., 2022). The magnitude of the viral load is then an important determinant to evaluate transmission rate, (Watanabe et al., 2010), and patients with higher viral load can be closely epidemiologically related (Marks et al., 2021). The Hill function has been widely adopted to link viral load and transmission risk for different diseases including influenza (cf. Handel and Rohani (2015)) and SARS-CoV-2 (cf. Heitzman-Breen and Ciupe (2022), Ke et al. (2020), and Goyal et al. (2021)). The transmission risk is split into contagiousness and infectiousness in Goyal et al. (2021), which is evaluated by the Hill function with the same parameters. In Ke et al. (2020), the probability of infection is defined as the chance that at least one virion seeds infection and they assume only a proportion of inhaled virus could arrive in the respiratory tract of the contact. Based on these assumptions, an exponential form dose–response model with a Michealis-Menten term representing the amount of virus shed from the upper respiratory tract is adopted in Ke et al. (2020). For the dose–response model developed by Ke et al. (2021), it can be simplified to a Hill function to link the viral load with the infectiousness if the composite parameter is sufficiently small. Furthermore, Ke et al. (2021) indicates that the infectiousness is sub-linear with the viral load and suggests that the logarithm of viral load is a better surrogate of infectiousness when data is given by RNA copies. Moreover, Haas et al. (2014) introduces a series of dose–response models under the competing risk framework for bacterial infections, and two models, the exponential and approximate beta-Poisson dose–response models, of Haas et al. (2014) are applied in Xu et al. (2023) to consider the transmission risk of SARS-CoV-2. Ejima et al. (2021) estimate the infection establishment threshold according to each patient, however, it is measured by RNA copies, which is not applicable in our case.

In this work, we also aim to develop an alternative derivation for a dose–response model. The simplified model developed in Xu et al. (2023) is adapted to reduce the viral dynamics to a stochastic differential equation (SDE) that only involves the virus state, from which we construct a boundary problem to evaluate the probability of infection. To our knowledge, the boundary problem approach has not been used in deriving dose–response models. Compared with our model that simplifies the system as one compartment, the work of Chen et al. (2022) developed a stochastic agent-based model that delicately incorporates the anatomy and physiology of respiratory tract (also cf. Aristotelous et al. (2022), Chen et al. (2023), Pearson et al. (2023), and Zhang et al. (2023), which extends the baseline model to more complicated physiological phenomena including viral transport, host immune defences, and infection kinetics in different locations such as alveolar, bronchial, and nasal compartments.). This stochastic model simulates how SARS-CoV-2 moves through and infects the respiratory tract prior to any immune response and predicts the outcomes after the inhalation of SARS-CoV-2. The nature of the agent-based model requires repeated simulations to obtain probability estimates, however, it is more flexible to further bridge with other biological details. In this paper, constructing a boundary problem allows us to obtain a closed-form solution for the probability of infection and provides direct parameter sensitivities including how the extinction probability depends on replication rate, initial viral load, etc. However, the boundary problem is based on simplification that omits some fine-scale spatial features and treats the system as a complete compartment.

This study then involves three extensions to the model proposed in Xu et al. (2023): (1) We consider early infection dynamics, (2) merge this with the stochastic fade out properties of the system to use evidence of infecting dose in model calibration, and (3) we extend the model used in the replication phase to include a smoothly increasing adaptive immune response.

2. Methods

Consider a contact who inhales a certain amount of virus during an exposure event. Whether this contact will develop an infection depends on the viral dynamics during the early phase of infection. Specifically, we define the early phase infection as the time between the inhalation and the time that the virus is above the detectable level in those cases that develop infection. During this early phase of infection, there are two independent events that may happen: viral adjustment and then replication. During the viral adjustment phase, the inhaled dose reduces so that only a portion of the virus remains in the host. After some time the residual virus successfully enters susceptible cells and starts to replicate, and if the viral load reaches the threshold for infection, the contact will develop an infection.

2.1. Viral adjustment phase

After inhalation, we assume that the virus will decay during the viral adjustment phase and only a small amount of the viruses will achieve viral colonisation. In this case, identifying the number of virus that survive is important to estimate the probability of subsequent infection. This is conceptually similar to the rapid deposition phase expected in bacterial infections (Heppell et al., 2017) but here deposition is only a single component of the adjustment process.

To simulate this parsimoniously, we assume that the virus will decay exponentially with respect to time:

$$D(t) = D_0 e^{-\alpha t} \tag{2.1}$$

for $t \in \mathbb{R}_+$. In (2.1), parameter $\alpha > 0$ measures the viral decay rate during the viral adjustment phase and D_0 is the initial dose the contact inhaled during the exposure. This model suggests that after inhalation, the virus will be exhaled during breathing or cleared by immune

response, and at $t = t^*$, a certain amount of virus, $D(t^*) = D_0 e^{-\alpha t^*}$, realises viral colonisation at the location of the infection.

A deterministic model would always predict some residual viral load that would cause infection after the switch to the replication phase (cf. the 'atto-fox' phenomena Mollison, 1991). Instead, we develop a stochastic version where the dynamics during the viral adjustment phase is given by:

$$dD_t = -\alpha D_t dt + \sqrt{\alpha D_t} dW_t \tag{2.2}$$

for $t \in [0, t^*]$ where t^* is the time the virus takes to get adjusted to the human body and the diffusion term allows D_t to hit 0. In this case, it is very important to understand the probability of clearance during the viral adjustment and what is the distribution of the viral load that successfully entered the susceptible cells. Due to the structure of (2.2), there is no analytical form of the probability of D_t hitting 0 before t^*, as the PDE of the corresponding boundary problem or time-space method (see cf. Pedersen and Peskir (2016)) has no analytical solution. Hence, we will carry out simulation to evaluate the viral shedding under the stochastic setting in the following analysis. Instead of the stochastic diffusion model in (2.2) a discrete event stochastic simulation could be developed. This was considered, see Supplementary material, but the results were not very different to the diffusion-based simulation. Moreover, we note that a unit value of PFU is not a single viable entity and so fractional amounts of PFU have biological meaning.

2.2. Viral replication phase

The simplified within-host model developed in Xu et al. (2023) provides a viral mechanism when viral load is above the detectable level, which is given by:

$$\begin{aligned} dX &= -\delta \frac{\rho}{\phi} XV, \\ dV &= \delta(\rho X - 1)V - \mu H(t-\tau)V, \end{aligned} \tag{2.3}$$

where $H(t-\tau)$ is a Heaviside function and τ is the time when the adaptive immunity response is activated. In (2.3), X represents the compartment of susceptible cells, while V represents the compartment of viral load. Furthermore, by the definition of Xu et al. (2023), the initial condition of X and V are $X(0) = 1$ and $V(0) = V_0$, and ρ represents the threshold parameter in the model (so deterministically if $\rho > 1$ the virus grows and if $\rho < 1$ it decays) whilst ϕ modifies the removal of susceptible cells. One of the advantages of this model is that it parsimonious, however, it is still not possible to distinguish between the depletion of susceptible cells and the increasing adaptive immune response based on observational data like that provided by the HCS alone.

We can relax the assumption in (2.3) that the adaptive immune response is a Heaviside step function so that the immune response grows logistically over some timescale T which controls the speed of immune response growth. We also recast the model parameters for future calibration. Defining $\rho = 1 + \theta/\nu$, $\delta = \nu\sigma/T$ and $\mu = \sigma/T$ for some parameters σ, θ and ν means we have a model

$$\begin{aligned} \dot{X} &= -\frac{(\theta+\nu)\sigma}{\phi T} XV, \\ \dot{V} &= \frac{\sigma}{T}(\theta X - \nu(1-X) - Y)V, \\ \dot{Y} &= \frac{Y(1-Y)}{T}. \end{aligned} \tag{2.4}$$

Note that the role of parameters σ, θ, and ν is to reparameterise the model, which has no biological meaning. The variable Y then is a non-dimensional representation of immune response scaling from a small contribution at initial time $t = 0$ to 1 as $t \to \infty$. Notice that when $X \sim 1$ and $Y \sim 0$ this system will grow exponentially in V with rate $r = \theta\sigma/T$, and when $X \sim 1$ and $Y \sim 1$ it will decay exponentially with rate $r_D = (1-\theta)\sigma/T$. Then introducing a time τ we may solve the adaptive immune response directly such that $Y_t = \theta(\theta + (1-\theta)e^{-(t-\tau)/T})^{-1}$ which means that at time τ the adaptive response has achieved θ of its eventual impact which also means that the parameter $\theta \in [0, 1]$.

We could solve this in the composite situation of both susceptible cell depletion and immune response increase. However, as noted in Xu et al. (2023) with (2.3) the contributing mechanism is unidentifiable in this scenario given the data provided from HCS. If we limit consideration to the case where $X \sim 1$ (so assume that $\phi \gg V(t)$ for all t) then τ is the time of peak viral load (noting that when $t = \tau$ we have $\dot{V} = 0$). The parameter τ then can be considered identical to the τ that appears in the Heaviside function in (2.3). We can define a time t_L representing the time at which the viral load is above some (known) detectable level (V_L) for the first time, meaning that

$$V(t; V_L, t_L, \tau, \theta, \sigma, T) = V_L \left(\frac{(\theta + (1-\theta)e^{(\tau - t_L)/T}) e^{\theta(t-t_L)/T}}{\theta e^{(t-t_L)/T} + (1-\theta)e^{(\tau-t_L)/T}} \right)^{\sigma}. \tag{2.5}$$

2.3. Probability of infection and boundary problems

To find the probability of infection during this replication phase, we introduce stochasticity into the viral dynamics in Eq. (2.4) to describe the heterogeneity of response across patients. Hence, the viral dynamics, V, after the viral adjustment is defined by the following SDE (assuming $Y = Y(t^*)$ and $X \sim 1$):

$$dV_t = \frac{\sigma}{T}(\theta - Y)V_t dt + \sqrt{\frac{\sigma}{T}(\theta + Y)V_t} dW_t \tag{2.6}$$

for $t \in [t^*, \infty)$ and $V_{t^*} = D(t^*) > 0$ is the amount of virus deposited at time t^*. Furthermore, we set that $\mathrm{E}_{t,v}(V_t) < \infty$ for any $(t, v) \in [t^*, \infty) \times \mathrm{R}$. After the virus deposited at $t^* > 0$, the contact will be infected if the viral load eventually reaches the threshold, $M > 0$, for infection, i.e. $V_t = M$ for some $t > t^*$, or the contact will clear the virus before it approaches to the threshold for infection, i.e. $V_t = 0$ for some $t > t^*$. Whilst we set $M = V_L$ the limit of detection we do not have to make this restriction but simply note that $M > V(t^*)$ for the rest of the paper to avoid regularity issue. The goal of this section is to find the relationship between the adjusted viral load, $D(t^*)$, and probability of infection $P_I(D_0)$ for a given dose D_0. Note that $D(t^*) = D_0 e^{-\alpha t^*}$ so we can link the probability of infection with initial dose D_0. During the viral replication phase, there are only two events will happen, infection and clearance, so we can define two stopping times:

$$\begin{aligned} \kappa_{\text{in}} &= \inf_t \{t > 0 | V_t = M\}, \\ \kappa_{\text{ex}} &= \inf_t \{t > 0 | V_t = 0\}. \end{aligned} \tag{2.7}$$

Finding the probability of infection is equivalent to calculating the probability of $\mathrm{P}(\kappa_{\text{in}} < \kappa_{\text{ex}})$. To estimate this probability, we first need to obtain the expectation $E_{V_*}(V_\kappa)$ as $E_{V_*}(V_\kappa) = M\mathrm{P}(\kappa_{\text{in}} < \kappa_{\text{ex}}) + 0\mathrm{P}(\kappa_{\text{in}} > \kappa_{\text{ex}}) = M\mathrm{P}(\kappa_{\text{in}} < \kappa_{\text{ex}})$, where $\kappa = \min\{\kappa_{in}, \kappa_{ex}\}$.

For SDE (2.6), we see that the drift term satisfies $(\sigma(\theta - Y)V/T)^2 = (\theta - Y)^2(\sigma V)^2/T^2 \le K(1 + |V|^2)$, and the diffusion term satisfies $\sqrt{(\theta + Y)\sigma V/T} \le K(1 + |V|)$ for some constant $K > 0$ (remember that $Y < \theta$ for $t < \tau$ so this condition will hold for times prior to the peak viral load). Based on the continuity and strict positivity of $(\theta - Y)^2 V^2$, the SDE (2.6) has an unique strong solution with strong markov property (cf. Stroock–Varadhan Theorem on Chapter V of Rogers and Williams (2000)). Define a value function $F(v) = E_v(V_\kappa)$, we can form the following boundary problem with infinite time horizon (cf. chapter 3 of Peskir and Shiryaev (2006)), which is given by:

$$\begin{aligned} &\hat{\mathcal{L}}_v F = 0 \\ &F(M) = M \\ &F(0) = 0 \end{aligned} \tag{2.8}$$

in which $\hat{\mathcal{L}}_v$ is the infinitesimal generator and $F(M) = M$ and $F(0) = 0$ describe the corresponding boundary conditions. Solving Eq. (2.8) will give $E_v(V_\kappa)$, hence, recalling $\mathbb{L}_v F = 0$, one has:

$$(\theta - Y)vF'(v) + \frac{1}{2}((\theta + Y)v)F''(v) = 0 \tag{2.9}$$

Table 1
Summary of key parameters used in within-host model and dose–response model of SARS-CoV-2 infection.

Parameter	Meaning/Role
D_0 (PFU)	Initial inhaled viral dose
α	Viral decay rate during the adjustment phase
t^* (d)	Duration of the adjustment phase (i.e. time until virus starts replicating)
$D(t^*)$ (PFU)	Adjusted viral load entering susceptible cells after adjustment phase
ϕ	Modifies the removal rate of susceptible cells
δ	Viral clearance rate
ρ	Threshold parameter for viral replication (i.e. virus grows if $\rho > 1$, decays if $\rho < 1$)
μ	Adaptive immune clearance rate
τ (d)	Time at which the adaptive immune response becomes active
θ	Internal reparameterisation variable with no direct biological meaning
ν	Internal reparameterisation variable with no direct biological meaning
σ	Internal reparameterisation variable with no direct biological meaning
T (d)	Timescale over which immune response grows logistically
t_L (d)	Time when viral load first exceeds the detectable limit (i.e. 5 PFU/mL)
Θ	Derived parameter that determines infection probability in dose–response model

(noting the factor σ/T drops out). Note that $Y \sim Y(t^*) = \theta(\theta + (1-\theta)e^{(\tau-t^*)/T})^{-1}$. Solving Eq. (2.9) gives:

$$F(v) = \frac{M(1-e^{-2\Theta v})}{1-e^{-2\Theta M}}, \tag{2.10}$$

where:

$$\Theta = \frac{(\theta - Y(t^*))}{(\theta + Y(t^*))} = \frac{(1-\theta)(e^{(\tau-t^*)/T}-1)}{1+\theta+(1-\theta)e^{(\tau-t^*)/T}}. \tag{2.11}$$

Since we have known that $E_v(V_\kappa) = M\mathrm{P}(\kappa_{\text{in}} < \kappa_{\text{ex}})$, the probability of infection during the replication phase can be easily obtained:

$$P_I(V_*) = \frac{(1-e^{-2\Theta V(t^*)})}{1-e^{-2\Theta M}}, \tag{2.12}$$

where $V(t^*)$ is the amount of residual virus following the adjustment phase. In Eq. (2.12), it is reasonable to assume that M varies for different patients and obtaining the actually value for M can be challenging, which leads to unidentifiability for parameter inference. Therefore, we would like to investigate what happens when M tends to infinity. Hence, when $M \to \infty$, the probability of infection is:

$$P_I(V(t_*)) = 1 - e^{-2\Theta V(t_*)}. \tag{2.13}$$

Note that (2.13) has the same form as the exponential dose response function. However, since $V(t_*) = D_0 e^{-\alpha t^*}$, Eq. (2.13) gives:

$$P_I(D_0) = 1 - e^{-2\Theta D_0 e^{-\alpha t^*}}, \tag{2.14}$$

which links the initial dose D_0 and the probability of infection with parameters arising from the model calibration to HCS data, though given an initial dose this is still of the form of the exponential dose–response function. In Table 1, we summarise the key parameters used in the within-host and dose–response models.

2.4. Parameter inference

As mentioned in the introduction, we will use the data from the HCS (cf. Killingley et al. (2022)). The data collected from this study involved throat and mid-turbinate swabs from 18 volunteers for the first 14 days after infection and was recorded by culture and qRNA. Since we only consider the potential of transmission risk in this paper, we will only use the culture data in the following part. First the replication phase model (2.5) is calibrated to the individual trajectories (with $V_L = 5$ PFU fixed) to identify parameters t_L, T, σ, τ and θ.

We perform approximate Bayesian computation-sequential Monte Carlo (ABC-SMC) in which a multivariate normal distribution with optimal local covariance matrix is adopted to pursue parameter inference (cf. Toni et al. (2009) and Minter and Retkute (2019)). For ABC-SMC, we set the distance function as:

$$d(M,O)^2 = \sum_{t\in T}\left(\log_{10}V^{(O)}(t) - \log_{10}V^{(M)}(t)\right)^2 \tag{2.15}$$

where the time points t are those in the set T where $V^{(O)} > V_L =$ and $V^{(O)}$ and $V^{(M)}$ represent the observations (from HCS) and simulated outputs respectively. We set 8 generations of iterations and collect 250 particles from iterations. During each iteration, we set the values calculated from the cost function from smallest to largest and choose the value of the 1st quartile as the tolerance level for the next iteration.

In this work, the prior distributions for the replication phase parameters are given by:

$$t_L \sim \text{Uniform}(\tilde{t}-1, \tilde{t}+1)\ \ T \sim \text{Uniform}(0,10)\ \ \tau \sim \text{Uniform}(t_L, 14)$$
$$\sigma \sim \text{Exp}(0.1)\ \ \theta \sim \text{Uniform}(0,1)$$

where $\tilde{t}$ is the last day that viral load stays undetectable after deliberate infection. This means the time of peak must be after or same as the time of earliest detection. In the supplementary material, Figures 5 and 6 show the posterior predictions (central estimate and 95% credible interval) and the observed data. Furthermore, in striving for more intuitive results, we merge the posterior distributions of each parameter assuming equal weighting to each sample, which is illustrated in Fig. 1.

However, the adjustment model has two further parameters (α and t^*). We assume that for some $t^* < t_L$ that $V(t) = 0$ for $t < t*$. We may then match this to the adjustment phase solution such that $V(t^*) = D_0 e^{-\alpha t^*}$ so for a choice of t^* we have

$$\alpha = \frac{1}{t^*}\ln\left(\frac{D_0}{V(t^*)}\right). \tag{2.16}$$

Then (2.14) enables us to obtain an estimate of t^* (given values of D_0 and $P_I(D_0)$) such that the following is satisfied

$$\begin{aligned} V(t^*) &= V_L\left(e^{\theta(t^*-t_L)/T}\frac{\theta+(1-\theta)e^{(\tau-t_L)/T}}{\theta e^{(t^*-t_L)/T}+(1-\theta)e^{(\tau-t_L)/T}}\right)^{\sigma} \\ &= -\frac{\ln(1-P_I(D_0))(1+\theta+(1-\theta)e^{(\tau-t^*)/T})}{2(1-\theta)(e^{(\tau-t^*)/T}-1)} \end{aligned} \tag{2.17}$$

Note that t^* appears a number of times in (2.17) and so we may solve this numerically. However, an approximate estimate can be derived by making the assumption that V is growing exponentially and that $\tau \gg t^*$ so that

$$t^* = t_L + \frac{T}{\theta\sigma}\ln\left[-\frac{\ln(1-P_I(D_0))}{2V_L}\right] \tag{2.18}$$

The Human Challenge Study tells us $D_0 = 55$ and that 18 out of 34 volunteers developed an infection so $P_I(D_0) = 18/34 = 0.53$ (Killingley et al., 2022). The uncertainty in α and t^* is conditional on the posterior distributions elicited from data calibration.

3. Results

3.1. Model calibration

We first calibrate the model (2.5) to the HCS and the merged posterior distributions for each of the parameters based on throat and

mid-turbinate data are illustrated in Fig. 1 (and the corresponding posterior predictions are illustrated in Supplementary material [Figures 5 and 6]). The red vertical lines on each panel show the 95% confidence interval on the merged posterior but as these are merged from a relatively small sample (18 volunteers) this should be treated as indicative only.

Note that the parameters T and σ appear fairly uni-modal and smooth for both sites, though the distribution of T is more narrow in the mid-turbinate than the throat. However, t_L and τ (both parameters sensitive to the location of the viral load in time) are more disjoint, due to the sample size of HCS, with the mid-turbinate having a wider range than parameter estimates from throat data. The parameter θ appears bi-modal on both sites and generally with similar shape.

We can unpack these marginal summaries by looking at the posterior distributions of each individual (Supplementary material Figure 7) but this is also seen in the bilateral correlation plots (Figs. 2 and 3). It is worth reflecting on the action the parameters are having in the model: t_L and τ act to locate the viral load in time, T acts to scale the viral load over time (relative to t_L and τ), σ scales the viral load magnitude while θ drives the shape. These plots also need a degree of care to interpret and are hard to briefly summarise, given that are a composite of 18 individual fits.

In Fig. 2 the parameter estimates appear to show the strongest degree of overall correlation between τ and t_L (larger τ suggests larger t_L) but looking at the individual parameter estimates by colour block this is less apparent (or may be negatively correlated). Fig. 3 does not show the same pattern of overall correlation for t_L with other parameters.

The stronger patterns of correlation are a correlation between T, τ and θ in both locations. Not only are they consistent between sites but they also have broadly consistent trends between individuals. The timescale of immune response (T) is positively correlated with the exponent for viral load (σ) for individuals and across the whole sample so larger values of T (slower immune response activation) correspond to larger values of σ (meaning potentially higher eventual viral concentration at peak). This does not mean that people with slower immune responses necessarily shed more (θ and τ would have some role in this too).

The interplay between the timing of the peak τ and θ appears more strongly in the throat than mid-turbinate but is consistent in both (and correlations in general are weaker in mid-turbinate). Individuals appear to cluster in two groups, one with low θ and high τ and *visa versa*, with the majority of individuals in the latter. Although the individual scatter in Figs. 2 and 3 shows a degree of complexity to this pattern this may be a tentative sign the people whose viral load peaks later have slower growth rates. This may not sound particularly interesting as slow growth would suggest a later peak but this is not strongly coupled with the magnitude of peak virus (driven by σ).

Based on the posterior distribution illustrated in Fig. 1, we can easily estimate the value of t^* as well as the value of $V(t^*)$ through Eqs. (2.18) and (2.17) which are shown in Fig. 4. Clearly we could have chosen to plot the estimate for α instead of $V(t^*)$ but felt that $V(t^*)$ was more intuitive. The majority of individuals then have an adjustment time between 0 and 3 days in both locations though about 3 individuals have longer adjustment time in mid-turbinate (about 5 or 7 days). This is not surprising due to the values of t_L derived in the previous section. However, the residual viral load at this time tends to be lower in mid-turbinate.

Apart from the difference in adjustment period, the adjusted viral load in mid-turbinate and throat show differences. In the left bottom of Fig. 4, the kernel density estimation of $V(t^*)$ of mid-turbinate shows that the actual viral load adjusted is around 0.5 to 1.6 PFU based on mid-turbinate data, which is a loss of 2 orders of magnitude from the initial dose, 55 PFU. For mid-turbinate, the adjustment rate is around 1%–3%. In the right bottom of Fig. 4, the adjusted viral load is around 0.5 to 2.5 PFU. This result could be indication that throat may be more susceptible to SARS-CoV-2 virus and more virus can survive viral adjustment or may be an artefact of the dosing regime of HCS. Overall, Fig. 4 indicates that a very small amount of virus retained in human body is enough to cause an infection.

3.2. Simulation of the stochastic viral adjustment phase

Due to the difficulty of finding the analytical solution for the probability of clearance during viral adjustment phase, we will carry out simulation to see the viral dynamics. The idea is that we first simulate the SDE (2.2) for $t \in [0, t^*]$. If D_t hits 0, we consider the virus is cleared before virus enters susceptible cells and the patient will not develop an infection. Otherwise, $V(t^*) > 0$ gives the adjusted viral load at t^*. For each patient, we use the mean value of the posterior distribution for each parameters, t_L, T, τ, θ and σ, from which we can easily calculate the value of α and t^* through Eqs. (2.16) and (2.18). For each patient, we simulate the corresponding SDE (2.2) for 30,000 times, from which we can receive the proportion of simulation that faded out during viral adjustment. Since we know that the Human Challenge Study indicates the overall viral clearance rate is 0.47, multiplying 0.47 with the proportion of clearance during viral adjustment will enable us to know the probability of clearance during viral adjustment and viral replication respectively. The results of our simulation are displayed in Table 2 and also in supplementary material Figures 8 and 9.

In Table 2, both mid-turbinate and throat show similar fade out probabilities in viral adjustment with mean 0.29 and 0.26 respectively. This means about 60% of clearance is achieved during the adjustment phase. For example patient A has 32% chance of not becoming a case due to the adjustment phase, then they had a residual viral load at start of replication phase that carried a 22% chance of stochastic fade out (conditional on virus surviving to replication and the overall 47% infection rate in volunteers).

4. Discussion

In this paper, we develop explicit mechanisms to explain viral dynamics in the first few days of infection *and* evaluate the probability of infection by deriving the dose–response model. Furthermore, we extend the viral load model by considering logistic growth in adaptive immune response. We fully appreciate these models are coarse simplifications of the true biological mechanisms but they enable us to interpret the available data.

The work of Wu et al. (2023) comes up with the two-step mechanism for Covid-19 infection. Wu et al. (2023) conducts an air–liquid interface culture of human nasal epithelium and notes that, despite plenty of virus initially present, only a very small fraction of cells were infected, nearly 3% by 24 h post-inoculation, but by 48 h post-infection nearly 80% of ciliated cells became infected. This two-step infection pattern suggests an initial period of viral ‘adjustment’ or ‘trapping’, followed by a surge of productive infection. Experiments in Wu et al. (2023) confirm that the mucus layer efficiently traps and delays the virus, and mucociliary clearance (MCC) eliminates infectious particles by coughing or swallowing. Furthermore, Wu et al. (2023) point out that the culture has a substantial kinetic delay (24–48 h), compared to tissue culture models, which was established as being linked to airway barrier function. Only after this delay can the virus breach the barrier and infect cells in large numbers. Our mathematical model does not directly incorporate the specific biological functions, however, there is conceptual compatibility between them. Specifically, the viral adjustment phase of the model can be seen as a simplified mathematical description and manifestation of early host-viral dynamics, including the interaction between the virus and the mucosal barrier, local immunity, etc., which is associated with the biological first step. The replication phase directly corresponds to the biological processes of viral replication and spread within cells, which is the second biological

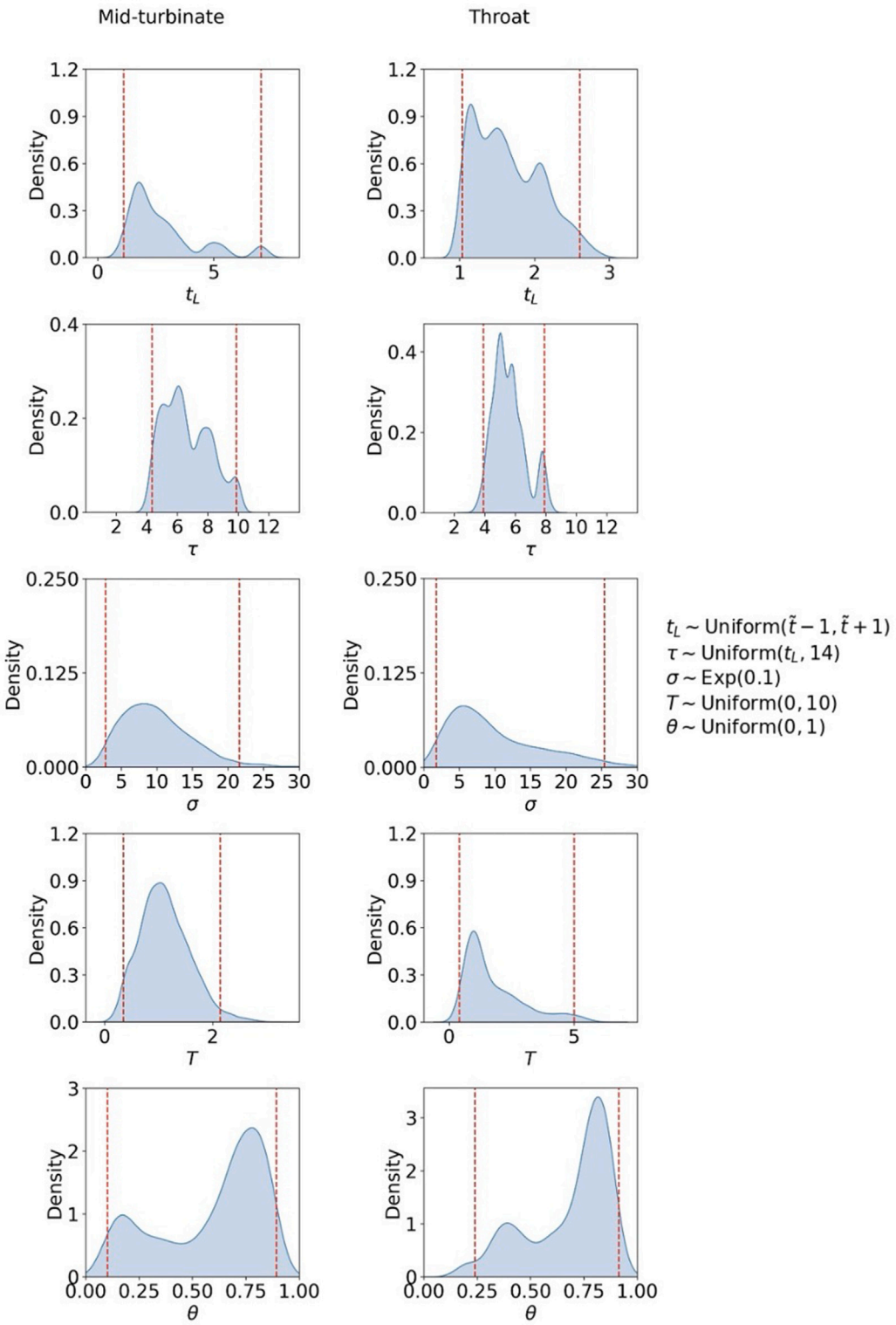

Fig. 1. Posterior distribution of parameter values from the result of ABC-SMC for Model (2.5) using mid-turbinate data and throat data (Killingley et al., 2022). The vertical dash lines represent the 2.5th and 97.5th percentiles for each parameter.

step. Overall, we believe that this biological two-step infection mechanism provides a deeper biological explanation which can complement and support the viral dynamic phenomena observed at the macro level by our mathematical model.

In another modelling work based on the HSC data (Iyaniwura et al., 2024), authors assume that the infection is initiated once one target cell enters the eclipse phase, incorporating more detailed biological processes into the model to interpret the viral growth kinetics.

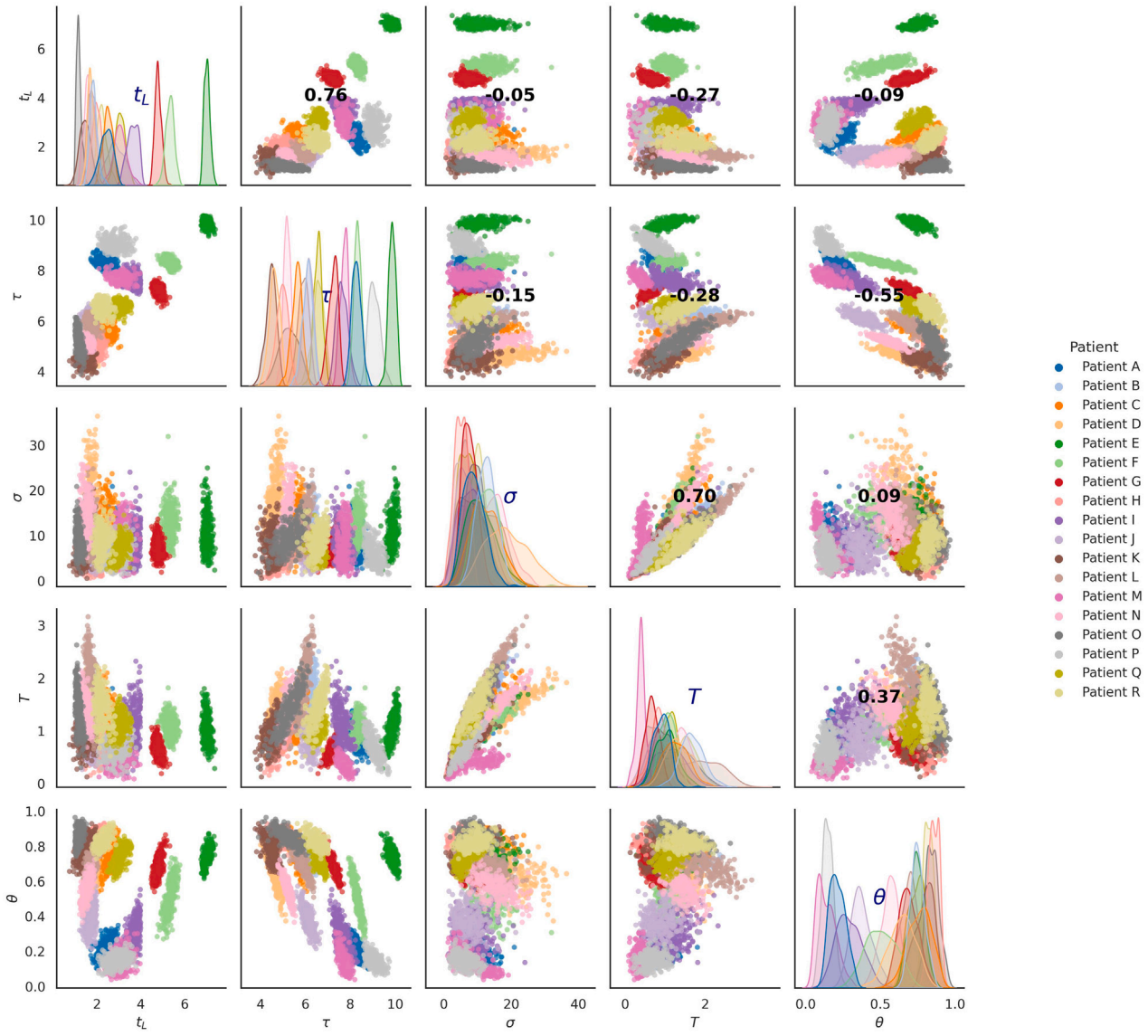

Fig. 2. Scatter plots illustrating a pair plot showing the relationships among parameters from parameter inference based on mid-turbinate data (Killingley et al., 2022). The diagonal plots show the distribution of each parameter, while the other plots illustrate the relationships between pairs of parameters. The bold numbers indicate the correlation strength between parameters.

Meanwhile, Iyaniwura et al. (2024) point out that there could be a gap (e.g., local stochastic infection and extinction) between the inoculation and the start of exponential growth, which is conceptually consistent with our assumption of the viral adjustment phase. Furthermore, the initial condition has been set as when one cell enters the eclipse phase since the exact number of virions that initiated infection is unknown. In this paper, our simplified mathematical models allow us to estimate the viral load that actually triggered the infection. These two approaches are not in conflict. In fact, we address different biological questions and these approaches could be integrated to more fully describe early infection uncertainty.

Based on Figs. 2 and 4, we notice that the mid-turbinate overall shows a broader window for viral adjustment: the virus will achieve viral adjustment within three days for nearly half of the patients. However, there are patients show a much longer period of adjustment phase ranging from 0 to 8 days, which is unsurprisingly consistent with the longer undetectable period in some patients (cf. Figure 5 in Appendix). Furthermore, the throat cases show a narrower length of adjustment phase up to 3 days. This result is consistent with the data measured in the work of Killingley et al. (2022), in which they found that the viral load in the throat significantly before nasal swabs turned positive. The virological mechanism behind this phenomenon is complicated. The work of Sungnak et al. (2020) points out that the expression of genes associated with immune functions is over-represented in nasal goblet 1 and 2 cells, and nasal ciliated 2 cells, which implies that nasal epithelial cells are conditioned to express these immune-associated genes to reduce viral susceptibility. Hence, one reasonable hypothesis is that the mid-turbinate is more resistant to SARS-CoV-2, which leads to a longer adjustment phase.

Furthermore, the estimated viral adjustment phase is centred around 1–2 days, which is consistent with the findings in Wu et al. (2023). However, we notice that in a few cases the mid-turbinate shows a much longer viral adjustment phase, which can extend to 6–8 days. Current research supports the hypothesis that the existence of an immune response and physical barrier traps the virus (cf. Sungnak et al. (2020), and Wu et al. (2023)) and delays the infection process. Also, the SARS-CoV-2 virus can remain stable for up to 21 days in biological fluids in controlled environment (Kwon et al., 2021). In another study, Becker et al. (2024) finds that mucociliary clearance inhibits pathogen penetration, indicating the virus remain extracellular

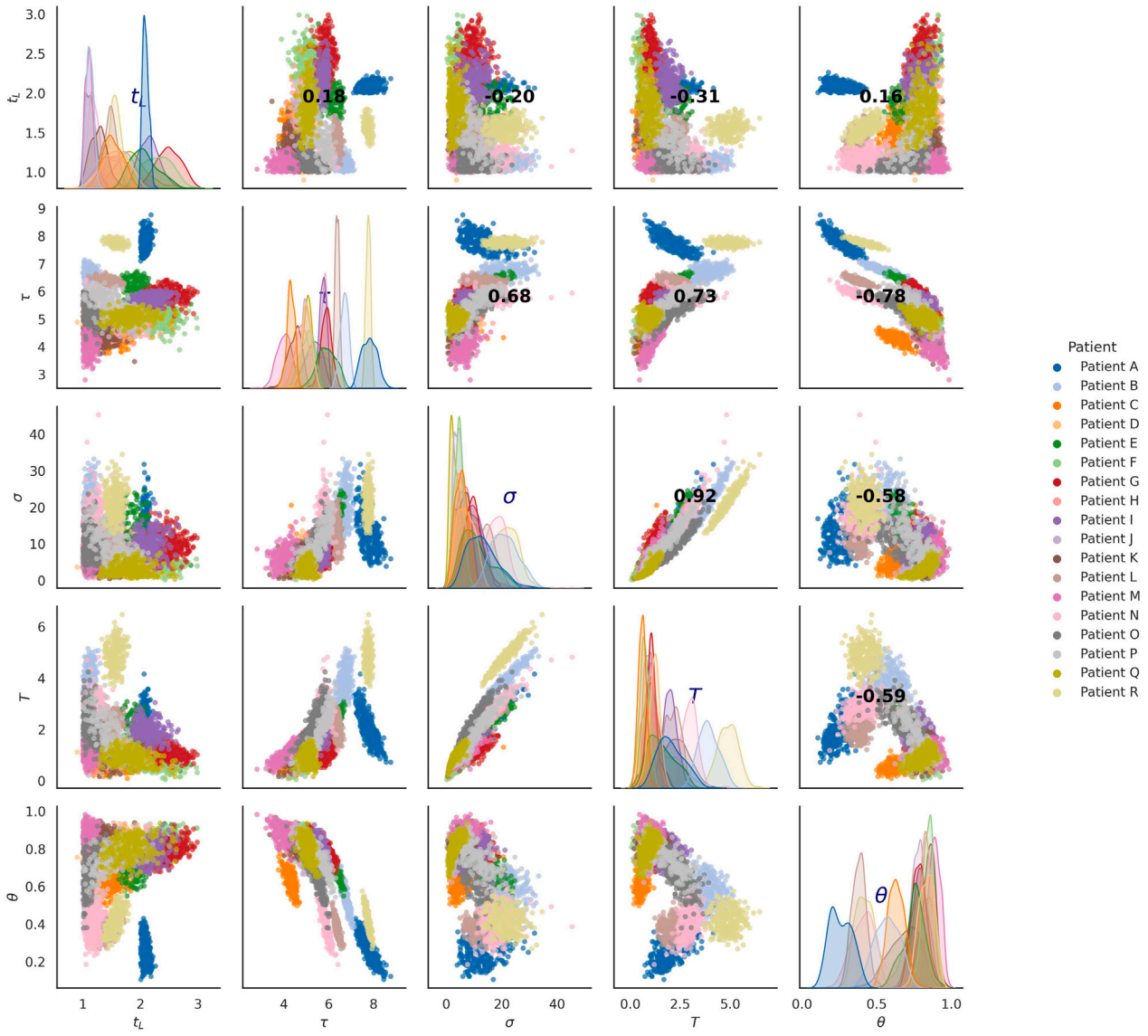

Fig. 3. Scatter plots illustrating a pair plot showing the relationships among parameters from parameter inference based on throat data (Killingley et al., 2022). The diagonal plots show the distribution of each parameter, while the other plots illustrate the relationships between pairs of parameters. The bold numbers indicate the correlation strength between parameters.

and trapped in secretions during early infection days. However, there is no direct *in vivo* evidence to measure how long SARS-CoV-2 virions can remain viable and infectious within airway secretions for extended periods even before cell entry. Another explanation for these longer viral adjustment phases predicted for a few patients is that it could be an artefact caused by the simplified modelling. Recall that the viral adjustment phase suggests that viral load will decay exponentially, however, we see that the data in Figure 5 and 6 does not show exponential decay. This is because we assume that the viral load decays so fast and drops below the detectable level before the measurement, which is consistent with most of the cases, except Patient E, F, and G in Figure 5. These three cases cause the extra long viral adjustment period in the mid-turbinate. Compared with the throat data of Patients E, F, and G, we see that the throat data of these three cases show that the infection was already established within 1–2 days. It is plausible to say that the actual viral adjustment of Patients E, F, and G in mid-turbinate can be short and the virus remains undetectable level for extra long days. The current simplified model cannot capture this behaviour. Biological studies also support this hypothesis; early detection of SARS-CoV-2 RNA in the throat but delayed detection in mid-turbinate swabs likely reflects a transient infection mentioned in Lindeboom et al. (2024), a study. Trans based on HCS. Transient infection represents the infection is successful but limited replicative infection has taken place, leading to viral loads that were borderline detectable (Lindeboom et al., 2024), which supports our hypothesis that viral adjustment happens in a very short period of time in these three patients but it is not possible to verify this with the data available.

The stochastic viral adjustment phase allows the virus to get completely cleared before it enters susceptible cells. This viral clearance can be caused by immune response or failure to deposit in a suitable site. As we have used the Human Challenge Study dose response observation that 47% of cases never have detectable virus, the stochastic viral adjustment mechanism reflects this strong chance that the virus will be cleared in either the viral adjustment or replication phases but suggests that in about 2/3rds of those that are not infected following exposure this is due to adjustment phase mechanisms. Of course, what we are calling the adjustment phase is much more complicated and may involve many potential bottlenecks or decay rates for which our model of $e^{-\alpha t_*}$ is a crude approximation.

However, based on Table 2, we can see that the throat shows an overall shorter t^* than that of mid-turbinate, which is consistent with

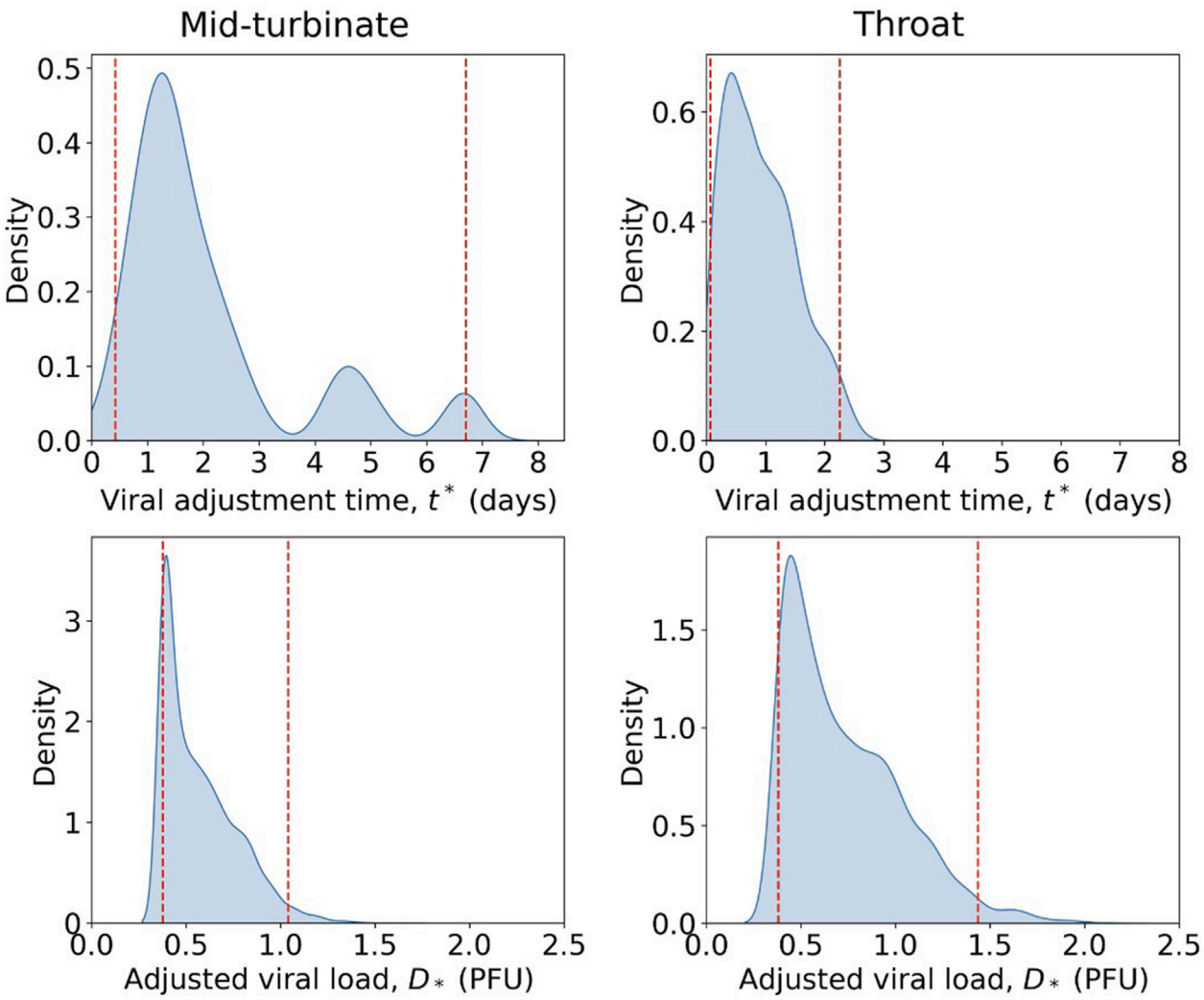

Fig. 4. The first column: approximate posterior distributions of viral adjustment time t^* and adjusted viral load $V(t^*)$ based on mid-turbinate data (Killingley et al., 2022). The Second column: approximate posterior distributions of viral adjustment time t^* and adjusted viral load $V(t^*)$ based on throat data (Killingley et al., 2022). Other parameter inference results can be seen in Fig. 1. The vertical dash lines represent the 2.5th and 97.5th percentiles for each parameter.

what we observed in the deterministic viral adjustment case. As we mentioned above, the mid-turbinate has immune-associated genes that may reduce viral susceptibility to SARS-CoV-2 infection (see Sungnak et al. (2020)) so the viral adjustment phase is longer. Also, the values of α of mid-turbinate have mean 3.07, and this is smaller than the value of α in the throat which is 6.03. This difference in α indicates that the throat may have a stronger immune response, which clears the virus faster, or people have a high chance to clear in their throat which reduces the viral load compared with say sneezing. Figures 8 and 9 in supplementary materials illustrated the distribution of viral load that adjusted to the body, in which we can see that in general, both mid-turbinate and throat have a similar range of values. However, mid-turbinate has a predominantly low viral load with limited variation, while throat has a more varied and higher range of adjusted viral load values, which is consistent with the previous conclusion of different viral dynamics in mid-turbinate and throat. It should be pointed out that in Figures 8 and 9, the value only means the viral load that enters the viral replication phase and does not mean the viral load can guarantee the infection, which should be distinguished from the deterministic case.

In this paper, we constructed a boundary problem based on the viral process, which leads to a dose–response model with exponential form. Upon our best knowledge, boundary problem has not previously been used to develop dose–response models and in this case returns the form expected from competing risk arguments but may allow for greater flexibility with further research. Under the competing risk framework of bacteria infection, Haas et al. (2014) develops a series of models to investigate dose–response relationships in different cases ranging from theoretical experimental scenarios to complicated real-world scenarios. In Haas et al. (2014) (also cf. Xu et al. (2023)), they assume that the virus is randomly distribution in the atmosphere around the inhaler and expected dose will be proportional to the amount of inhaled air. Whilst of similar mathematical form, the competing risk derivation is designed for pooled data so assumes that all patients are homogeneous given a specific dose while Model (2.14) enables consideration of the heterogeneity of individuals based on each set of the viral load data.

The viral replication model proposed in this study explains the data as well as conventional SIV-type models or models with more structured models for adaptive immune response. This model has 5 parameters, two are directly intuitive: time of detection and time of peak (t_L and τ respectively). The others (θ, T and σ) have an interpretation from model derivation in terms of the relative differences between timescales but they can also be considered as functions of the growth rate (i.e. $\theta\sigma/T$), decay rate (i.e. $(1-\theta)\sigma/T$) and peak viral load, see Supplementary B. This means the parameters are identifiable provided supporting data grows and then decays.

The striking finding is that the parameter θ shows signs of bimodality in the sample of volunteers. This is a clear feature of this sample but

Table 2
Simulated values for viral adjustment time t^*, viral decay rate α, fade out rate in adjustment, and Clearance rate in viral replication based on the posterior distribution in Fig. 1.

Results of simulation based on mid-turbinate data			
Patient No.	t^*	α	Fade out probability during adjustment
A	1.13	4.40	0.68
B	1.59	3.08	0.66
C	2.74	1.68	0.55
D	1.82	2.59	0.60
E	6.67	0.70	0.57
F	4.55	1.07	0.64
G	4.96	0.93	0.55
H	1.54	3.04	0.60
I	2.18	2.27	0.66
J	1.01	4.87	0.66
K	0.96	4.88	0.60
L	1.39	3.48	0.64
M	2.44	2.02	0.68
N	1.02	4.79	0.66
O	0.66	6.45	0.43
P	1.10	4.53	0.68
Q	2.59	1.84	0.62
R	1.78	2.62	0.57
Results of simulation based on throat data			
Patient No.	t^*	α	Fade out probability during adjustment
A	0.29	12.45	0.64
B	0.76	5.36	0.34
C	1.24	3.71	0.55
D	0.76	6.19	0.60
E	1.36	3.57	0.64
F	1.66	2.80	0.57
G	1.74	2.80	0.64
H	1.34	3.45	0.55
I	0.78	6.17	0.64
J	1.48	3.16	0.57
K	0.29	15.83	0.53
L	0.43	10.80	0.55
M	0.77	4.97	0.23
N	0.89	4.61	0.36
O	0.92	4.10	0.21
P	1.44	3.25	0.57
Q	1.65	2.63	0.45
R	0.32	12.75	0.36

it is not clear if this is an artefact of a relatively small sample (so more volunteers would have produced a more unimodal posterior combined sample) or a genuine feature. The estimates for t_L and τ appear to be multi-modal but as a result of the sample size of volunteers and that more participants might be expected to smooth these merged posteriors out further. However, the shape of posterior for θ appears structurally different particularly in mid turbinate sample.

The parameter θ is the growth rate divided by the sum of growth and decay rates ($\theta = r/(r+r_D)$). So slow growth with fast decay would lead to smaller values of θ, fast growth and slow decay values closer to 1 and balanced growth and decay values close to 0.5. From Fig. 2, in the mid-turbinate, those samples with smaller θ appear to exhibit later times of peak (τ) as might be expected for relatively slow growth (and consistent values of t_L). However, those with faster growth than decay exhibit a wider range of peak and detection times. It is noteworthy too that those volunteers with the highest eventual viral load in mid-turbinate (J and M) are in this cluster. This pattern is less clear in throat data.

In this work, we have made several necessary simplifications to capture the early infection dynamics of SARS-CoV-2. One key assumption treating the early viral adjustment phase as a single exponential decay, which is a clear simplification of a complex biological process such as airway mucus and mucociliary clearance, etc. (cf. Tosta (2021) for details of respiratory defence barriers). It is mathematically convenient, however, it may not capture the true timing and impact of each biological mechanism. Another limitation is the lack of experimental data during the very early phase of infection (prior to detectable viral load), which restricts model validation in that regime. As a result, the model behaviours and conclusions are essentially inferred rather than directly confirmed, which, on one level, fills in a gap that experiments cannot observe due to detection thresholds. However, without empirical measurements, we must rely on assumptions (e.g. an exponential clearance rate, clearance before replication, etc.) to describe early dynamics, and we cannot rigorously verify that this assumed form reflects reality. Overall, considering these simplifications and data limitations, the insights yielded by our model should be interpreted with appropriate caution.

CRediT authorship contribution statement

Jingsi Xu: Writing – review & editing, Writing – original draft, Methodology, Formal analysis, Conceptualization. **Martín López-García:** Writing – review & editing, Supervision, Methodology, Conceptualization. **Thomas House:** Writing – review & editing, Supervision, Methodology, Conceptualization. **Ian Hall:** Writing – review & editing, Supervision, Formal analysis, Conceptualization.

Funding information

JX, MLG, TH, and IH were supported by the TRACK: Transport Risk Assessment for COVID Knowledge project - EPSRC, United Kingdom, EP/V032658/1 -. JX, TH, and IH were supported by the Wellcome Trust Grant - 227438/Z/23/Z.

Declaration of competing interest

The authors have no competing interests to declare.

Acknowledgements

We would like to thank the TRACK project team for their contributions. This work was supported by the EPSRC (EP/V032658/1-) and the Wellcome Trust (227438/Z/23/Z).

Appendix A. Supplementary data

Supplementary material related to this article can be found online at https://doi.org/10.1016/j.epidem.2025.100843.

References

Abuin, P., Anderson, A., Ferramosca, A., Hernandez-Vargas, E.A., Gonzalez, A.H., 2020. Characterization of SARS-CoV-2 dynamics in the host. Annu. Rev. Control. 50, 457–468.
Aristotelous, A.C., Chen, A., Forest, M.G., 2022. A hybrid discrete-continuum model of immune responses to SARS-CoV-2 infection in the lung alveolar region, with a focus on interferon induced innate response. J. Theoret. Biol. 555, 111293.
Baccam, P., Beauchemin, C., Macken, C.A., Hayden, F.G., Perelson, A.S., 2006. Kinetics of influenza A virus infection in humans. J. Virol. 80 (15), 7590–7599.
Beauchemin, C.A., McSharry, J.J., Drusano, G.L., Nguyen, J.T., Went, G.T., Ribeiro, R.M., Perelson, A.S., 2008. Modeling amantadine treatment of influenza A virus in vitro. J. Theoret. Biol. 254 (2), 439–451.
Becker, M.E., Martin-Sancho, L., Simons, L.M., McRaven, M.D., Chanda, S.K., Hultquist, J.F., Hope, T.J., 2024. Live imaging of airway epithelium reveals that mucociliary clearance modulates SARS-CoV-2 spread. Nat. Commun. 15 (1), 9480.
Challenger, J.D., Foo, C.Y., Wu, Y., Yan, A.W., Marjaneh, M.M., Liew, F., Thwaites, R.S., Okell, L.C., Cunnington, A.J., 2022. Modelling upper respiratory viral load dynamics of SARS-CoV-2. BMC Med. 20 (1), 1–20.
Chen, A., Wessler, T., Daftari, K., Hinton, K., Boucher, R.C., Pickles, R., Freeman, R., Lai, S.K., Forest, M.G., 2022. Modeling insights into SARS-CoV-2 respiratory tract infections prior to immune protection. Biophys. J. 121 (9), 1619–1631.
Chen, A., Wessler, T., Forest, M.G., 2023. Antibody protection from SARS-CoV-2 respiratory tract exposure and infection. J. Theoret. Biol. 557, 111334.

Du, S.Q., Yuan, W., 2020. Mathematical modeling of interaction between innate and adaptive immune responses in COVID-19 and implications for viral pathogenesis. J. Med. Virol. 92 (9), 1615–1628.
Ejima, K., Kim, K.S., Ludema, C., Bento, A.I., Iwanami, S., Fujita, Y., Ohashi, H., Koizumi, Y., Watashi, K., Aihara, K., et al., 2021. Estimation of the incubation period of COVID-19 using viral load data. Epidemics 35, 100454.
Fajnzylber, J., Regan, J., Coxen, K., Corry, H., Wong, C., Rosenthal, A., Worrall, D., Giguel, F., Piechocka-Trocha, A., Atyeo, C., et al., 2020. SARS-CoV-2 viral load is associated with increased disease severity and mortality. Nat. Commun. 11 (1), 1–9.
Ghosh, I., 2021. Within host dynamics of SARS-CoV-2 in humans: Modeling immune responses and antiviral treatments. SN Comput. Sci. 2 (6), 482.
Gonçalves, A., Maisonnasse, P., Donati, F., Albert, M., Behillil, S., Contreras, V., et al., 2021. SARS-CoV-2 viral dynamics in non-human primates. PLoS Comput. Biol. 17 (3), e1008785.
Goyal, A., Cardozo-Ojeda, E.F., Schiffer, J.T., 2020. Potency and timing of antiviral therapy as determinants of duration of SARS-CoV-2 shedding and intensity of inflammatory response. Sci. Adv. 6 (47), eabc7112.
Goyal, A., Reeves, D.B., Cardozo-Ojeda, E.F., Schiffer, J.T., Mayer, B.T., 2021. Viral load and contact heterogeneity predict SARS-CoV-2 transmission and super-spreading events. Elife.
Haas, C.N., Rose, J.B., Gerba, C.P., 2014. Quantitative Microbial Risk Assessment. John Wiley & Sons.
Handel, A., Rohani, P., 2015. Crossing the scale from within-host infection dynamics to between-host transmission fitness: a discussion of current assumptions and knowledge. Phil. Trans. R. Soc. B 370 (1675), 20140302.
Heitzman-Breen, N., Ciupe, S.M., 2022. Modeling within-host and aerosol dynamics of SARS-CoV-2: The relationship with infectiousness. PLoS Comput. Biol. 18 (8), e1009997.
Heppell, C.W., Egan, J.R., Hall, I., 2017. A human time dose response model for Q fever. Epidemics.
Hernandez-Vargas, E.A., Velasco-Hernandez, J.X., 2020. In-host mathematical modelling of COVID-19 in humans. Annu. Rev. Control. 50, 448–456.
Holder, B.P., Simon, P., Liao, L.E., Abed, Y., Bouhy, X., Beauchemin, C.A., Boivin, G., 2011. Assessing the in vitro fitness of an oseltamivir-resistant seasonal A/H1N1 influenza strain using a mathematical model. PloS One 6 (3), e14767.
Iyaniwura, S.A., Ribeiro, R.M., Zitzmann, C., Phan, T., Ke, R., Perelson, A.S., 2024. The kinetics of SARS-CoV-2 infection based on a human challenge study. Proc. Natl. Acad. Sci. 121 (46), e2406303121.
Ke, R., Zitzmann, C., Ho, D.D., Ribeiro, R.M., Perelson, A.S., 2021. In vivo kinetics of SARS-CoV-2 infection and its relationship with a person's infectiousness. Proc. Natl. Acad. Sci. 118 (49), e2111477118.
Ke, R., Zitzmann, C., Ribeiro, R.M., Perelson, A.S., 2020. Kinetics of SARS-CoV-2 infection in the human upper and lower respiratory tracts and their relationship with infectiousness. MedRXiv.
Killingley, B., Mann, A.J., Kalinova, M., Boyers, A., Goonawardane, N., Zhou, J., Lindsell, K., Hare, S.S., Brown, J., Frise, R., et al., 2022. Safety, tolerability and viral kinetics during SARS-CoV-2 human challenge in young adults. Nature Med. 28 (5), 1031–1041.
Kwon, T., Gaudreault, N.N., Richt, J.A., 2021. Seasonal stability of SARS-CoV-2 in biological fluids. Pathogens 10 (5), 540.
Li, J., Wu, J., Zhang, J., Tang, L., Mei, H., Hu, Y., Li, F., 2022. A multicompartment mathematical model based on host immunity for dissecting COVID-19 heterogeneity. Heliyon e09488.
Li, C., Xu, J., Liu, J., Zhou, Y., 2020. The within-host viral kinetics of SARS-CoV-2. BioRxiv.
Lindeboom, R.G., Worlock, K.B., Dratva, L.M., Yoshida, M., Scobie, D., Wagstaffe, H.R., Richardson, L., Wilbrey-Clark, A., Barnes, J.L., Kretschmer, L., et al., 2024. Human SARS-CoV-2 challenge uncovers local and systemic response dynamics. Nature 631 (8019), 189–198.
Madelain, V., Baize, S., Jacquot, F., Reynard, S., Fizet, A., Barron, S., Solas, C., Lacarelle, B., Carbonnelle, C., Mentré, F., et al., 2018. Ebola viral dynamics in nonhuman primates provides insights into virus immuno-pathogenesis and antiviral strategies. Nat. Commun. 9 (1), 1–11.
Marks, M., Millat-Martinez, P., Ouchi, D., h Roberts, C., Alemany, A., Corbacho-Monné, M., Ubals, M., Tobias, A., Tebé, C., Ballana, E., et al., 2021. Transmission of COVID-19 in 282 clusters in Catalonia, Spain: a cohort study. Lancet Infect. Dis. 21 (5), 629–636.
Minter, A., Retkute, R., 2019. Approximate Bayesian Computation for infectious disease modelling. Epidemics 29, 100368.
Mollison, D., 1991. Dependence of epidemic and population velocities on basic parameters. Math. Biosci. 107 (2), 255–287.
Pearson, J., Wessler, T., Chen, A., Boucher, R.C., Freeman, R., Lai, S.K., Pickles, R., Forest, M.G., 2023. Modeling identifies variability in SARS-CoV-2 uptake and eclipse phase by infected cells as principal drivers of extreme variability in nasal viral load in the 48 h post infection. J. Theoret. Biol. 565, 111470.
Pedersen, J.L., Peskir, G., 2016. Optimal mean–variance selling strategies. Math. Financ. Econ. 10, 203–220.
Peskir, G., Shiryaev, A., 2006. Optimal Stopping and Free-Boundary Problems. Springer.
Pujadas, E., Chaudhry, F., McBride, R., Richter, F., Zhao, S., Wajnberg, A., Nadkarni, G., Glicksberg, B.S., Houldsworth, J., Cordon-Cardo, C., 2020. SARS-CoV-2 viral load predicts COVID-19 mortality. Lancet Respir. Med. 8 (9), e70.
Rogers, L.C.G., Williams, D., 2000. Diffusions, Markov Processes and Martingales: Volume 2, Itô Calculus, vol. 2, Cambridge University Press.
Sadria, M., Layton, A.T., 2021. Modeling within-host SARS-CoV-2 infection dynamics and potential treatments. Viruses 13 (6), 1141.
Sungnak, W., Huang, N., Bécavin, C., Berg, M., Queen, R., Litvinukova, M., Talavera-López, C., Maatz, H., Reichart, D., Sampaziotis, F., et al., 2020. SARS-CoV-2 entry factors are highly expressed in nasal epithelial cells together with innate immune genes. Nature Med. 26 (5), 681–687.
Toni, T., Welch, D., Strelkowa, N., Ipsen, A., Stumpf, M., 2009. Approximate Bayesian computation scheme for parameter inference and model selection in dynamical systems. J. R. Soc. Interface 6 (31), 187–202.
Tosta, E., 2021. The seven constitutive respiratory defense barriers against SARS-CoV-2 infection. Rev. Soc. Bras. Med. Trop. 54, e0461–2021.
Wang, S., Pan, Y., Wang, Q., Miao, H., Brown, A.N., Rong, L., 2020. Modeling the viral dynamics of SARS-CoV-2 infection. Math. Biosci. 328, 108438.
Watanabe, T., Bartrand, T.A., Weir, M.H., Omura, T., Haas, C.N., 2010. Development of a dose-response model for SARS coronavirus. Risk Anal. 1129–1138.
Williams, B., Carruthers, J., Gillard, J.J., Lythe, G., Perelson, A.S., Ribeiro, R.M., Molina-París, C., López-García, M., 2024. The reproduction number and its probability distribution for stochastic viral dynamics. J. R. Soc. Interface 21 (210), 20230400.
Williamson, B.N., Feldmann, F., Schwarz, B., Meade-White, K., Porter, D.P., Schulz, J., Van Doremalen, N., Leighton, I., Yinda, C.K., Pérez-Pérez, L., et al., 2020. Clinical benefit of remdesivir in rhesus macaques infected with SARS-CoV-2. Nature 585 (7824), 273–276.
Wu, C.-T., Lidsky, P.V., Xiao, Y., Cheng, R., Lee, I.T., Nakayama, T., Jiang, S., He, W., Demeter, J., Knight, M.G., et al., 2023. SARS-CoV-2 replication in airway epithelia requires motile cilia and microvillar reprogramming. Cell 186 (1), 112–130.
Xu, J., Carruthers, J., Finnie, T., Hall, I., 2023. Simplified within-host and Dose–response Models of SARS-CoV-2. J. Theoret. Biol. 111447.
Zhang, L., Cao, H., Medlin, K., Pearson, J., Aristotelous, A.C., Chen, A., Wessler, T., Forest, M.G., 2023. Computational modeling insights into extreme heterogeneity in COVID-19 nasal swab data. Viruses 16 (1), 69.